Limnol. Oceanogr., 53(5, part 2), 2008, 2226–2236
© 2008, by the American Society of Limnology and Oceanography, Inc.

Net community production in the deep euphotic zone of the subtropical North Pacific gyre from glider surveys

David Nicholson, Steven Emerson, and Charles C. Eriksen
School of Oceanography, University of Washington, Seattle Washington 98195

Abstract

Seagliders, deployed through most of 2005 in the subtropical North Pacific gyre, made measurements of temperature, salinity, and dissolved oxygen to quantify net community production (NCP) at Station A Long-Term Oligotrophic Habitat Assessment (ALOHA) of the Hawaii Ocean Time-series (HOT) using an oxygen mass balance approach. A 'bowtie'-shaped pattern, 50 km by 50 km in size was repeatedly traversed at two week intervals with the goal of observing the influence of Rossby waves and eddies on the productivity of the study region. Rossby waves and eddies in the region cause a vertical displacement of isopycnal depth of $\sim\pm 50$ m at the base of the euphotic zone. Shoaling of isopycnals is demonstrated to drive productivity in the deep euphotic zone. Four mesoscale shoaling events were observed between February and November in 2005. During each event when isopycnals shoaled, oxygen concentrations on isopycnals increased, fluorescence in the deep euphotic zone was higher, and net community production was elevated. Productivity in the deep euphotic zone was strongly influenced by Rossby waves and eddies, but this influence was not observed to extend into the mixed layer.

Introduction

The net community production (NCP) of the ocean is an important aspect of the carbon cycle and a primary control on the partial pressure of carbon dioxide (pCO_2) of the atmosphere. The processes that regulate NCP, the amount that gross primary productivity (GPP) exceeds respiration (R), are poorly understood. The net biological production of oxygen (O_2) can be used to quantify NCP and is a powerful tracer of biological processes in the ocean surface.

Geochemical studies suggest that annually, the euphotic zone of the subtropical gyres have a positive NCP and produce an excess of organic carbon which subsequently is exported to the deep ocean (e.g., Spitzer and Jenkins 1989; Gruber et al. 1998; Quay and Stutsman 2003; Hamme and Emerson 2006). In vivo studies of short term GPP and R using bottle incubations suggest the opposite, that R exceeds GPP (Duarte and Agusti 1998; del Giorgio and Duarte 2002; Williams et al. 2004). One hypothesis reconciling these observations is that NCP occurs in brief bursts of 'productivity events' (Emerson et al. 2002) and that net heterotrophic conditions exist between events (McAndrew et al. 2007). Eddies and Rossby waves may be the triggers that drive these events.

Acknowledgments

We would like to thank Craig Lee at the University of Washington Applied Physics Lab; he provided great assistance in the objective analysis. Thanks to Charles Stump and members of the Seaglider team at the University of Washington as well as the scientists and technicians of the Hawaii Ocean Time Series Program for help in deploying, operating, and recovering Seagliders and collecting ancillary data. Our thanks also go to two anonymous reviewers for their insightful comments. The National Science Foundation (NSF-OCE 0223372) and the National Aeronautics and Space Administration (NASA) Earth Systems Science Graduate Fellowship program provided funding support.

Because primary productivity in the subtropical gyres of the ocean is probably nitrate and phosphate limited, any physical processes that bring nutrients into the euphotic zone can trigger NCP and organic matter export. Cyclonic eddies can elevate isopycnals, bringing nutrients from deeper waters into the euphotic zone, driving new production (McGillicuddy et al. 2003; Sweeney et al. 2003). In the subtropical North Pacific, westward propagating Rossby waves cause oscillations in sea-surface dynamic height that can be observed in altimetry data (Chiswell 1994). Rossby waves and eddies, while displacing sea-surface height (SSH) by only a few centimeters, often displace thermocline isopycnals by tens of meters. These oscillations may provide a significant flux of nutrients into the euphotic zone (Sakamoto et al. 2004) and drive productivity events.

The ability to observe these episodic events and their impact on NCP requires continuous observation over many months. The autonomous Seaglider is an optimal platform for such a study. We use Seaglider measurements to determine NCP using the oxygen mass balance approach (e.g., Emerson et al. 1997; Hamme and Emerson 2006).

Biological production of O_2 in the ocean is stoichiometrically related to carbon uptake by the ratio $\Delta O_2 : \Delta C = 1.45$ during nitrate-based photosynthesis (Hedges et al. 2002; Anderson 1995). Regenerated production based on ammonium (NH_4^+) uptake has a ratio of $\Delta O_2 : \Delta C = 1.1$ (Laws 1991). We suspect that new production is primarily driven by nitrate and that $\Delta O_2 : \Delta C = 1.45$ is an appropriate ratio to convert net biological O_2 production to NCP of carbon.

In this paper, we focus on NCP in the deep euphotic zone because this zone is most directly influenced by nutrient injections from below. In the mixed layer, nutrients are more likely to be supplied by other sources, such as nitrogen fixation. Furthermore, uncertainties in gas exchange and bubble injection processes make it difficult to constrain the mixed-layer NCP using only O_2 gas measurements. Mixed-layer NCP for our study site is calculated in Emerson et al. (2008) using in situ mooring measurements of nitrogen and

O_2. Mixed-layer NCP was not observed to correlate with the timing of mesoscale shoaling events.

Seaglider O_2 measurements centered on Station A Long-Term Oligotrophic Habitat Assessment (ALOHA; 22°45′N, 158°W) of the Hawaii Ocean Time-series and the Hawaii Air–sea Logging Experiment (HALE-ALOHA) mooring (Moore et al. unpubl.; 22°46′N, 158°5.5′W) during 2005 were used to investigate controls on NCP in the deep euphotic zone. We used shipboard Winkler titration measurements to calibrate Seabird and Aanderaa O_2 sensors and to evaluate their accuracy and precision during Seaglider use. An objective analysis (OA) was used to identify the primary time and length scales of temperature (T), salinity (S), and O_2 variability and to create a gridded data set to be used for mass balance calculations. Using OA-mapped Seaglider data we calculated net biological O_2 production for the deep euphotic zone (below the mixed layer) in the vicinity of Station ALOHA during 2005. Finally, we investigated the role of four observed mesocale shoaling events in driving NCP in the deep euphotic zone of the subtropical North Pacific gyre.

Methods

The Seaglider—The Seaglider is a small, autonomous sampling platform developed at the University of Washington collaboratively between the School of Oceanography and the Applied Physics Laboratory (Eriksen et al. 2001). Seagliders are battery powered, using buoyancy control and wing lift to propel the glider forward at speed of ~0.25 m s^{-1}. They can be deployed for up to 6 months at a time and have a range of thousands of kilometers because of very low power consumption. Seagliders use global positioning system (GPS) fixes acquired at the sea surface to navigate, and they use the Iridium satellite network to communicate control commands and return data in near real time. Measurements include the concentration of dissolved O_2 ($[O_2]$), T, S, fluorescence, optical backscatter, and depth-averaged currents.

Seagliders for this project were equipped with a custom Seabird conductivity–temperature–depth (CTD) sensor to measure S, T, and pressure, a Seabird SBE-43 $[O_2]$ sensor, an Aanderaa Optode 3830 $[O_2]$ sensor (optode), and Wetlabs BB2SF fluorescence and optical backscatter. S and T sensors were mounted on a sail protruding from the top of the Seaglider, between the wings. The SBE43 and optode were mounted atop and beneath the aft portion of the fairing, respectively.

Three Seaglider deployment periods were used in this study to collect data through much of 2005 at Station ALOHA. Deployments of Seaglider 021 spanned 16 February 2005 to 22 May 2005 and 15 August 2005 to 13 November 2005 while Seaglider 020 was deployed from 22 May 2005 to 24 July 2005. The 3-week gap in data coverage from late July to mid-August occurred when Seaglider 020 malfunctioned and was lost. During the study, Seagliders continuously traversed a 50 km by 50 km 'bowtie'-shaped pattern centered on Station ALOHA (Fig. 1). The 'bowtie' was traversed about once every 2 weeks, totaling 17 repetitions over the study period. The size of the 'bowtie' was chosen as a tradeoff between the spatial coverage and the repeat interval for the flight path, with the particular goal of being able to resolve mesoscale variability. Each dive cycle, which transects 5 km to 7 km horizontally and reaches a maximum depth of 1000 m, takes ~5 h to complete in these missions. Measurements were collected at variable time intervals: every 10 s from 0 m to 40 m, every 5 s from 40 m to 80 m depth, every 10 s from 80 m to 150 m, every 20 s from 150 m to 300 m, and every 40 s below 300 m. This resulted in measurements being recorded at a depth resolution finer than 1 m in the mixed layer and thermocline and as coarse as every 5 m below the thermocline during both dive and climb.

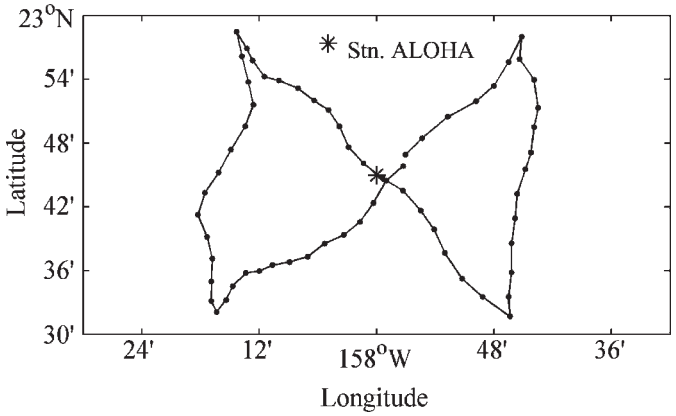

Fig. 1. Surface path of Seaglider 021 from day 226 to day 240 showing one lap around the 'bowtie'-shaped flight path. Dots represent locations where the Seaglider was at the surface.

O_2 measurement—In order to calculate an O_2 mass balance, we must have a high degree of confidence in O_2 measurements made by the O_2 sensors (Seabird SBE43 and Aanderaa Optode 3830). The SBE43 sensor is a modified Clark polargraphic electrode (Clark et al. 1953). O_2 diffuses through a sensor membrane and is electrochemically reduced in the sensor, producing a current that is proportional to $[O_2]$. The Aanderaa optode sensor makes an optical measurement by exciting a luminiferous porphyrin foil with a monochromatic pulse of light from a light emitting diode (LED). The quenching time of the resulting fluorescence is dependent on $[O_2]$ (Tengberg et al. 2006). The inherently different methods used by the sensors result in each having distinct advantages and disadvantages.

In the configuration used on Seagliders, the SBE43 is operated without a pump in order to conserve energy. At slow flow speeds, this results in anomalously low readings due to depletion of O_2 by the sensor near the sensing membrane surface. Another issue is the stability of the SBE43 over the long deployment periods of the Seaglider. Over the duration of each of the three deployments spanning several months, the SBE43 showed a drift toward lower O_2 measurements when compared to the optode and Winkler measurements. This rate of drift was variable, but on the order of 5% to 10% (10 μmol kg^{-1} to 20 μmol kg^{-1}) over 100 d of deployment. Drift in SBE43 sensors could be due to either biofouling, depletion of analyte, or another unidentified issue.

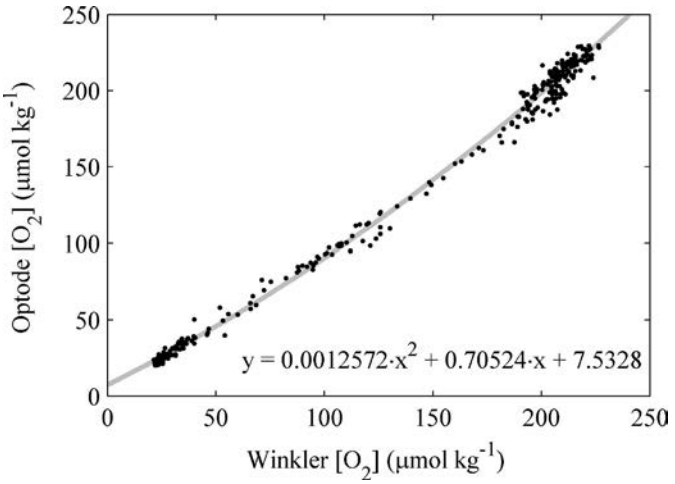

Fig. 2. Seaglider optode O_2 measurements are compared to Winkler titration measurements taken during HOT cruises and mooring deployment cruises. Each point represents a Winkler measurement and the Seaglider optode measurement that was closest in space and time to when the Winkler sample was taken. The quadratic regression ($y = ax^2 + bx + c$) from all calibration data from February 2005 through November 2005 was used to correct the optode sensor ($r^2 = 0.996$). Standard error for a, b, and c are 8.46×10^{-05}, 2.13×10^{-2}, and 9.33×10^{-1}, respectively.

The Aanderaa optode sensor operates on a principle that does not consume O_2 or analyte and thus is not susceptible to flow speed dependence and sensor drift (Körtzinger 2005). Biofouling, which can affect both sensors, is the most likely cause of drift over long deployments. This problem is less severe than observed in mooring applications because the Seaglider spends most of its time below the euphotic zone. The optode sensor showed no sign of drift when compared to Winkler measurements over the 9 months of deployment. Seaglider 021, equipped with the same optode sensor, was stable from its initial February deployment through the end of its second deployment in November, without requiring any recalibration between deployments (data not shown). The optode on glider 020 showed similar stability over its shorter deployment.

Calibration of the Aanderaa optode sensor was accomplished during the study by using Winkler titrations on 337 samples taken during nine HOT and mooring deployment cruises. In 2005, HOT Winkler measurements had an average precision of ±0.18% (http://hahana.soest.hawaii.edu/hot/methods/oxygen.html; accessed June 2008). Optode observations were compared to Winkler titration O_2 measurements by choosing the Seaglider dive closest in time and location to each Winkler titration profile. The Seaglider dive chosen was always within 5 km and 4 d of the Winkler profile. Winkler titration water samples were then matched to the Seaglider optode measurement made on the same isotherm.

The optode vs. Winkler measurements indicate a nonlinear response of the optode sensor (Fig. 2). We therefore use quadratic fit for calibration to correct for the nonlinear response observed in the optode. This nonlinearity was consistently observed between the two gliders and between dive and climb data. The optode also has a slower response time as compared to the SBE43, resulting in fast changes in O_2 being somewhat smoothed. A correction for first-order lag is used to better capture spikes in O_2 profiles such that

$$[O_2]_{\text{corrected}} = [O_2] + \tau \frac{d[O_2]}{dt} \quad (1)$$

To best match the shape and depth span of O_2 features in SBE-43 profiles, a value of $\tau = 30$ s is used. This correction also improves the match of profiles taken during dive and ascent.

After calibration the standard deviation of error for the all calibration points for the optode is ±4.2 μmol kg^{-1}, or ~2% of saturation. For measurements taken in the mixed layer, the optode precision after calibration is ±1.9 μmol kg^{-1}, or <1% of saturation. Residuals are normally distributed. A portion of the observed error may be due to real differences between Winkler and Seaglider measurements. Even within the span of several hours, between the dive and climb cycle of the Seaglider, real O_2 features on the order of 5–10 μmol kg^{-1} have been observed to develop in the thermocline. Because of an offset of a few kilometers and/or a few days between Seaglider optode and Winkler measurements, some real differences in the O_2 concentration might be expected and may contribute to the observed error level.

Results

Objective analysis methods—Over the course of the three deployments, Seagliders made ~1100 dives and measurements at >860,000 locations, of which >390,000 were in the upper 200 m. In order to make mass balance calculations and quantitative assessments, measurements must be interpolated to a regular grid. This is done using an OA to map Seaglider measurements to a regular grid, assigning a value to each grid point and produce error estimates for the gridded fields of S, T, and O_2. (Bretherton et al. 1976; LeTraon 1990). The OA is a means to map mesoscale variations of a property that are superimposed on a background mean state. We define our mean state as a linear (in time and space) least-squares fit to the data to be mapped. T, S, and O_2 fields are mapped onto both isobaric and isopycnic surfaces. Depth-gridded maps were made at each 5 m interval from 2.5 m to 997.5 m. Maps of density surfaces were created for $\sigma_\theta = 22.5$–27.5 at intervals of 0.05 σ_θ units. Horizontal grid spacing is 1 km in both east–west and north–south directions. A map is created for each depth and density surface, covering the 50 km by 50 km study domain and for each 2-d interval, from day 50 through day 314 in 2005. These maps for each surface are stacked along the depth dimension to form a four-dimensional array ($[x, y, z, t]$ or $[x, y, \sigma_\theta, t]$).

The value at each grid point in the objective analysis is determined to be a linear combination of nearby measurements

$$\phi'_g = \sum_{i=1}^{N} p_i \phi'_i \quad (2)$$

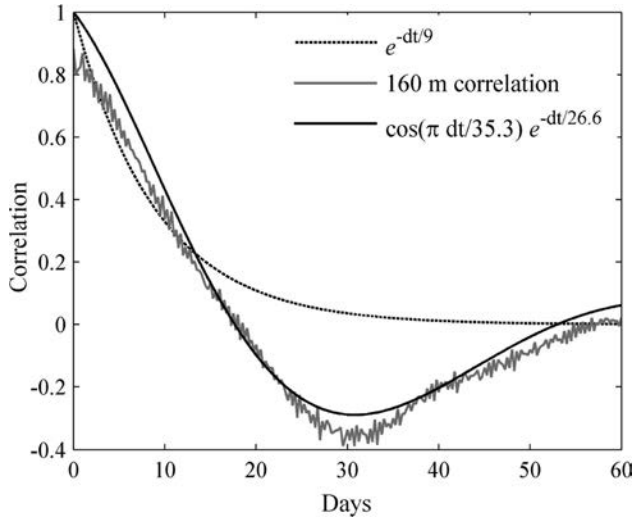

Fig. 3. Temperature correlation as a function of time from HA mooring thermister at 160 m (gray). The solid black line represents a best fit using a cosine times exponential functional form and dashed black line is an exponential fit. The solid black line fit captures the region of negative correlation between 30 d and 50 d, but both fits have the same correlation 1/*e* time scale of ~9 d.

where $\phi' = \phi - \phi_{\text{mean}}$, ϕ'_g is the grid location to be mapped and ϕ'_i are the measured values with a mean state subtracted and p_i are weighting coefficients. The weighting coefficients, p_i can be determined by minimizing the normalized mean-squared error, ε.

$$\varepsilon = \overline{\left(\phi'_g - \sum_{i=1}^{N} p_i \phi'_i\right)^2} \Big/ \phi'^2_g \tag{3}$$

Measurements taken close (in time and space) to the mapping location are expected to have similar values and therefore to be highly correlated to the mapping grid point. The result is that observations that are highly correlated (close) to the grid point location are given a large weighting coefficient, p_i, while poorly correlated (far away) observations are given small weighting coefficients. When we differentiate ε to minimize the normalized mean-squared error we get a set of *i* linear equations that can be solved to assign the weighting coefficients, *p*.

$$\frac{\partial \varepsilon}{\partial p_i} = 2r_{gi} + 2\sum_{j=1}^{N} p_j r_{ij} = 0, \text{ where } r_{gi} = \frac{\overline{\phi'_g \phi'_i}}{\overline{\phi'^2_g}}, \quad r_{ij} = \frac{\overline{\phi'_i \phi'_j}}{\overline{\phi'^2_g}}. \tag{4}$$

In the above equation, r_{gi} is the correlation coefficient between grid point and measurement location and r_{ij} is the correlation coefficient between measurement locations. Because the value we are trying to map, ϕ'_g, is unknown, we cannot calculate r_{gi} explicitly. Instead we assume that *r*, the correlation coefficient, is a function only of spatial separation and temporal lag between measurements. The further away in time and space a measurement is from the mapping location, the lower the expected correlation. We define the correlation time scale and length scales to be the lag (s) or separation (km) between measurements at which the correlation drops to 1/*e*.

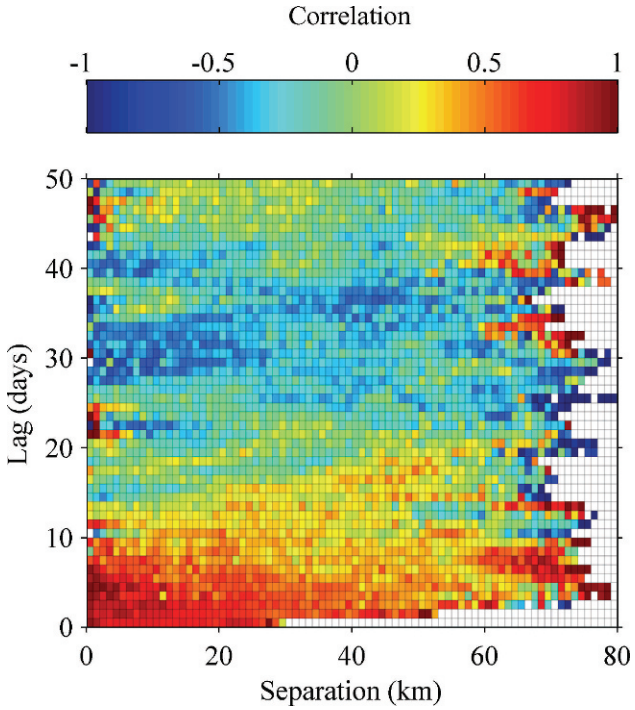

Fig. 4. A correlation map of temperature at a depth of 100 m from binned Seaglider data. Each grid box represents all pairs of measurements made at 100 m that are separated in space and time by the coordinates of the given grid box. Colors indicate how well correlated the pairs within each grid box are. Correlation of 1 indicates the paired measurements have the same difference from the mean state.

OA-correlation scales on depth surfaces—We use temperature data from 160 meters at the HALE-ALOHA mooring to isolate the correlation as a function of time lag only (Fig. 3). Functional form of the time dependent correlation was chosen so that the negatively correlated region at 20 d to 50 d of lag could be described by r_t:

$$r_t = \cos(\pi\, dt/T_1) \times e^{-dt/T_2}. \tag{5}$$

This functional form provides a much better fit to mooring data than does a simple exponential or Gaussian functional form (Fig. 3). Time and length scales of correlation were also determined from Seaglider data alone and agreed well with the correlation time scale determined from the mooring data. We therefore feel comfortable using Seaglider data alone to calculate correlation time and length scales for S and O_2.

Seaglider data was used to calculate correlation as a function of spatial separation and temporal lag by binning all possible pairs of Seaglider observations into lag and separation bins of 1 km by 1 d in size. The correlation coefficient was then determined from Seaglider measure-

ments for each bin and mapped as shown in Fig. 4. As we expect, these empirically determined correlation coefficients are highest for small lags and separations and then decrease as the lag and separation between measurements increases.

We then fit a smooth continuous function to the pattern of how correlation varies with space and time such that the correlation, r is

$$r = e^{-(dx/X_1)^2} \times \cos(\pi\, dt/T_1) \times e^{-dt/T_2} \quad (6)$$

where X_1, T_1, and T_2 are the length and time fit coefficients. For temperature mapped onto depth surfaces, for example, $X_1 = 53$ km, $T_1 = 35.3$ d, and $T_2 = 26.6$ d (Table 1). Equation 6 is the product of the time component of correlation, r_t (Eq. 5) and of the space component, r_s where

$$r_s = e^{-(dx/X_1)^2} \quad (7)$$

Correlation in space and time is considered to be isotropic and a function only of separation and lag. We define the length and time scales of correlation as the spatial separation and temporal lag at which r_s and r_t, respectively drop to a value of $1/e$. Fit parameters (X_1, T_1, and T_2 from Eq. 6) as well as the correlation scales are summarized in Table 1.

Correlation scales were determined from Seaglider data at a 100-m depth, corresponding to the deep euphotic zone. For temperature mapped on depth surfaces, the length scale of 53 km indicates that temperature anomalies are well correlated within a 53 km radius. The time coefficients show that this correlation lasts for about ±8.4 d. These characteristic scales of variability for T are dictated by mesoscale variations in the depth of isotherms. Cyclonic or anticyclonic flow brings anomalously cold or warm water to a given depth, as isotherms are displaced upward or downward, respectively. Rossby waves typically have wavelengths longer than ~600 km (Chelton and Schlax 1996; Polito and Liu 2003). The correlation length scale for a sine wave is ~20% of the wavelength, so Seaglider data with the observed 53-km–length scale would suggest mesoscale variability with an average wavelength of ~250 km, shorter than the typical Rossby wave. The mesoscale field near Station ALOHA is composed of a combination of Rossby waves and smaller-scale eddies in the region (Sakamoto et al. 2004). The superposition of these signals may result in the observed shorter-length scale. The

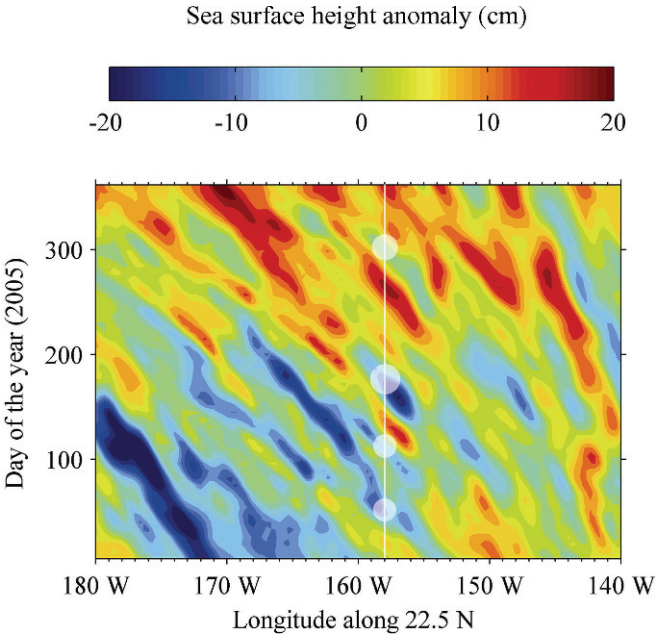

Fig. 5. Hovmöller diagram of sea-surface height anomaly (cm) at latitude 22.6°N through 2005. The east-to-west propagating features (seen as diagonals from lower right to upper left) are a signature of Rossby waves. The vertical white line shows the longitude of Station Aloha (158°W). White circles mark four periods of low SSH. Altimeter products were produced by Segment Sol multimissions d'ALTimétrie, d'Orbitographie et de localisation précise/Data Unification and Altimeter Combination System (Ssalto/Duacs) and distributed by Archiving, Validation and Interpretation of Satellite Oceanographic data (Aviso), with support from Centre National d'études Spatiales (Cnes).

westward-propagating signals seen in the SSH data are unambiguous indicators of the influence of Rossby waves. Sakamoto et al. (2004) reports that 62% of the variance in the SSH field can be explained by Rossby waves.

Rossby waves propagated across the Pacific at the latitude of Station ALOHA covering ~20–25° longitude during 2005 (Fig. 5). This equates to a translational speed of about 5.5 km d^{-1} to 7 km d^{-1}. This would mean that the peak of a Rossby wave would cross the 50 km domain of this study in ~7–9 d, which is consistent with the temporal scale calculated by the objective analysis (Table 1). OA results

Table 1. Fit parameters (X_1, T_1, T_2) and correlation length and time scales for OA-mapped Seaglider data on depth and density surfaces. Length and time scales are determined by the separation or lag at which correlation drops to $1/e$. Scales are determined at 100 m for depth surfaces and on $\sigma_\theta = 24.3$ for density surfaces. The standard deviation, σ, for each property [°C, salinity (S) and μmol kg^{-1} for temperature (T), S, and oxygen (O_2), respectively] represents the amount these properties vary on depth and density surfaces.

Properties mapped onto depth surfaces				$r = e^{-(dx/X_1)^2} \cos(\pi\, dt/T_1) e^{-dt/T_2}$		
	X_1 (km)	T_1 (d)	T_2 (d)	Length scale (km)	Time scale (d)	σ
T	53.0	35.3	26.6	53.0	8.4	1.24
S	30.8	20.5	25.8	30.8	7.0	0.077
O_2	27.1	20.8	33.4	27.1	7.3	3.27
Properties mapped onto density surfaces				$r = e^{-(dx/X_1)^2} e^{-(dt/T_1)^2}$		
	X_1 (km)	T_1 (d)	T_2 (d)	Length scale (km)	Time scale (d)	σ
T	24.0	8.4	–	24.0	8.4	0.11
S	24.0	8.4	–	24.0	8.4	0.041
O_2	32.6	7.9	–	32.6	7.9	5.62

are consistent with Rossby waves being a primary form of mesoscale variability in our study region. This does not, however rule out the influence of other types of eddies.

S and dissolved O_2 both have shorter length scales at a 100-m depth than does T (Table 1). This indicates that these properties vary on scales smaller than that of the eddy-Rossby signal. At 160 m, deeper in the thermocline, the decorrelation length scale for both S and T was 50 km (data not shown), suggesting that deeper in the thermocline, isopycnal motion may be the dominant control on both S and T variations. At 100 m, S variations may also be influenced by mixed-layer dynamics and evaporation and precipitation forcing at the surface. The combination of these effects resulted in the observed correlation length scale of 30.8 km (Table 1). O_2 variability may be influenced by patchiness in biological productivity at scales smaller than that of the eddy–Rossby variability.

Objective analysis correlation scales on isopycnals—Because mooring data cannot be collected on isopycnal surfaces, Seaglider data were used to calculate length and time scales of correlation such that

$$r_\sigma = e^{-(dx/X_1)^2} \times e^{-(dt/T_1)^2} \quad (8)$$

Data were fit with a simple Gaussian shape without the cosine component used for depth surfaces, because this provided a better least-squares fit. Length and time correlation scales were calculated for T, S, and O_2 on density surfaces (Table 1). T and S mapped on density surfaces had small standard deviations ($\sigma_T = 0.11^\circ C$, $\sigma_S = 0.041$), varying much less on density surfaces than on depth surfaces (Table 1). Because T and S determine density, they covary on density surface maps. Due to the small signal of T and S on density surfaces, it is difficult to determine the accuracy and physical significance of the derived length and time scales. O_2, however, shows a standard deviation on density surfaces ($\sigma = 5.62$ μmol kg^{-1}) that is somewhat larger in magnitude to that on depth surfaces ($\sigma = 3.27$ μmol kg^{-1}). As isopycnals are displaced vertically in the water column, they move through depths with different photosynthesis : respiration balances, causing O_2 concentration to vary on isopycnal surfaces (*see* Discussion).

Mapped T, S, and O_2 fields—The major structure in T, S, O_2, and O_2-saturation anomaly fields can be seen in the mapped properties at Station ALOHA (Fig. 6). Mixed-layer depth reaches a maximum of >100 m in March and early April, then shoals to as shallow as 25 m in late April, after which the mixed layer slowly deepens through the rest of the study period. Isopycnals below the mixed layer show large displacements of >50 m from their mean depths. For example, $\sigma_\theta = 24.30$ has a mean depth of 118 m, but ranges from ~65 m to 175 m. The mixed-layer depth and the depth of $\sigma_\theta = 24.30$ (Fig. 6) are the upper and lower bounds of what we define as the deep euphotic zone. During 2005, the passage of several mesoscale events is manifest in displacements of isopycnals over a time scales of weeks to months. Four isopycnal shoaling events were observed during the study period (Fig. 5).

Mixed-layer depth was calculated from Seaglider dives and was defined as the depth at which density reached a value 0.15 kg m^{-3} greater than the mean density of the 5–15 m depth. Mixed-layer depth was calculated for each Seaglider dive and ascent to create a time series for mixed-layer depth. The time series was then filtered with a low-pass Butterworth filter with a cutoff frequency of ~0.07 d^{-1}. This produced a smoothed record of mixed-layer depth and removed short-term variability and noise. The filtered mixed-layer depth was used in mass balance calculations and shown in plots.

For T, the dominant feature in the mixed layer is a seasonal cycle of about 4°C, with variability of T below the mixed layer controlled primarily by variations in the depth of isopycnals (Fig. 6A). For S, the primary feature was a subsurface S maximum that persisted throughout the year, varying in depth from <50 m to ~150 m (Fig. 6B). The source of this maximum is an evaporation maximum minus a precipitation maximum to the north of Station ALOHA (Seckel 1968). This high-S water is subducted, then advected to the subsurface at Station ALOHA. While variable in depth, this subsurface maximum remains centered on $\sigma_\theta = 24.30$. The primary [O_2] signal in the upper ocean is a subsurface maximum that develops in spring and persists through fall located directly below the mixed layer (Fig. 6C). [O_2] in the mixed layer increased during the first 60 d of study period and decreased after that from late April 2005 through November 2005. The subsurface [O_2] maximum is associated with an O_2 saturation anomaly in the same location that reaches levels exceeding 5% supersaturated (Fig. 6D). The O_2 saturation anomaly was close to 0 (saturated) at the surface at the beginning of the study period. As the year progressed, surface saturation anomaly increased, peaking at ~2% during the summer. Through the late fall, both surface saturation and the subsurface maxima moderated back toward equilibrium.

OA gridded data also provided information about the spatial structure of properties near Station ALOHA. This spatial variability was visualized by placing slice planes through the gridded output. The maps of [O_2] and the O_2-saturation anomaly are shown for day 182 in Fig. 7. Properties are visualized by projecting the gridded data onto two diagonal planes that span the study volume at right angles. This projection shows some of the spatial variability of O_2 across the domain.

Objective analysis error estimation—It is important to know the error level associated with the OA-gridded product for quantitative use of the gridded data. The OA estimates error as a percentage of variance in the mean state-subtracted signal. This is done at each grid point location based on the weighting coefficients and distance of measurements from the grid location. This error estimate is multiplied by the variance at each depth or σ_θ level to arrive at an error estimate in the units of the property being mapped.

Error estimates were calculated for each grid point as described in Eq. 3. Error at a given mapping location is a function of the proximity (in time and space) of that location to where Seaglider measurements where made and

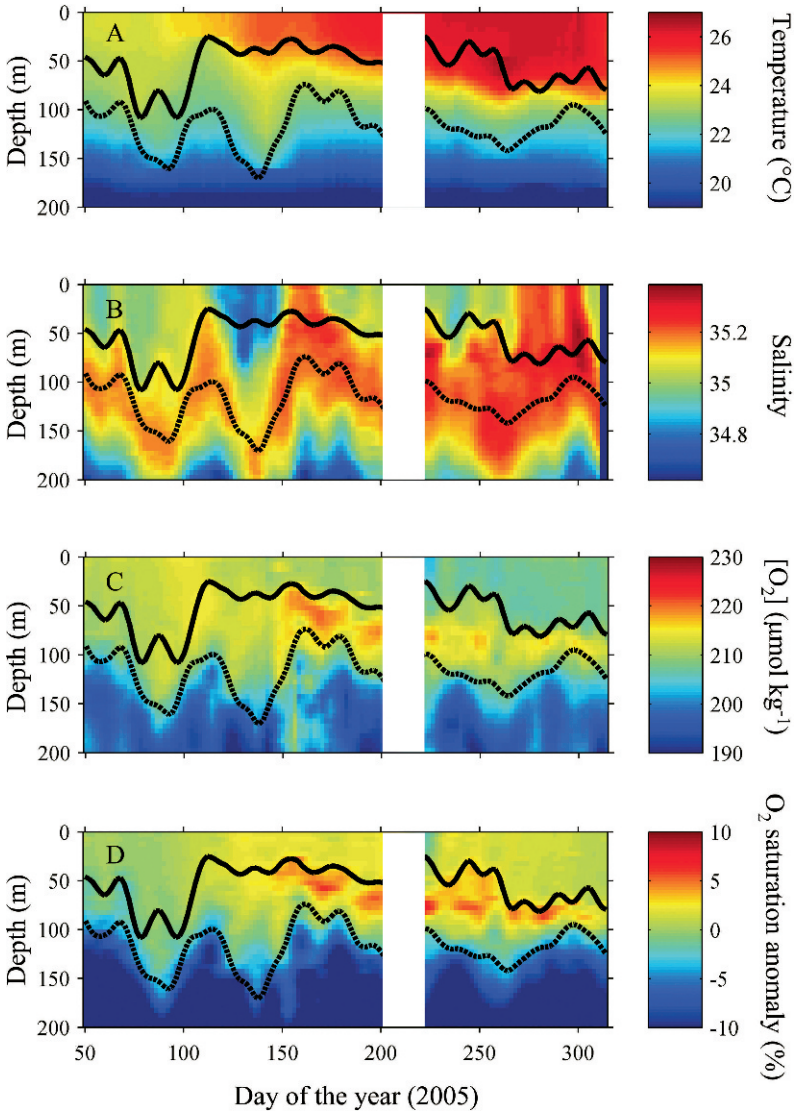

Fig. 6. (A) OA-mapped temperature (°C), (B) salinity, (C) dissolved O_2 (μmol kg^{-1}) and (D) O_2-saturation anomaly (percent) averaged over the 50 km by 50 km extent in the upper 200 m. The black line indicates mixed layer depth and the dashed black line is the depth of σ_θ = 24.30.

the variance of the property at the depth of the given mapping location. For example, Fig. 7A shows [O_2] and the associated error estimate for day 182. Around day 182, the Seaglider was near Station ALOHA traveling from southeast to northwest, so error was highest in the southwest and northeast corners, furthest from where the Seaglider was in the days before and after day 182. In depth, error is highest below 100 m in the thermocline, where [O_2] is most variable, and lowest in the mixed layer where there is low variability in [O_2].

Discussion

Seasonal O_2 variations—The average [O_2] of the upper 100 m showed a seasonal cycle, increasing from day 50 through day 110, from an average of 210 μmol kg^{-1} to 215 μmol kg^{-1} and then decreasing from day 110 through the end of the study period, around day 315. This cycle in O_2 is controlled by two competing processes. Net biological O_2 production occurs through the year at Station ALOHA and drives the surface ocean towards a supersaturated state. At the same time, warming from February through September decreases the equilibrium O_2 solubility of the water, driving O_2 out of the ocean surface via gas exchange to the atmosphere. Deepening of the mixed layer from 25 m to 75 m enhances this process by entraining water with excess O_2 from biological O_2 production below the mixed layer, bringing it into communication with the atmosphere.

During the first part of the year, biological O_2 production dominates and the average [O_2] increases. After day 110, loss of O_2 due to gas exchange dominates, lowering the average [O_2]. Entrainment enhances the gas exchange loss by eroding the subsurface O_2 maximum. By the end of the study period in November the subsurface O_2

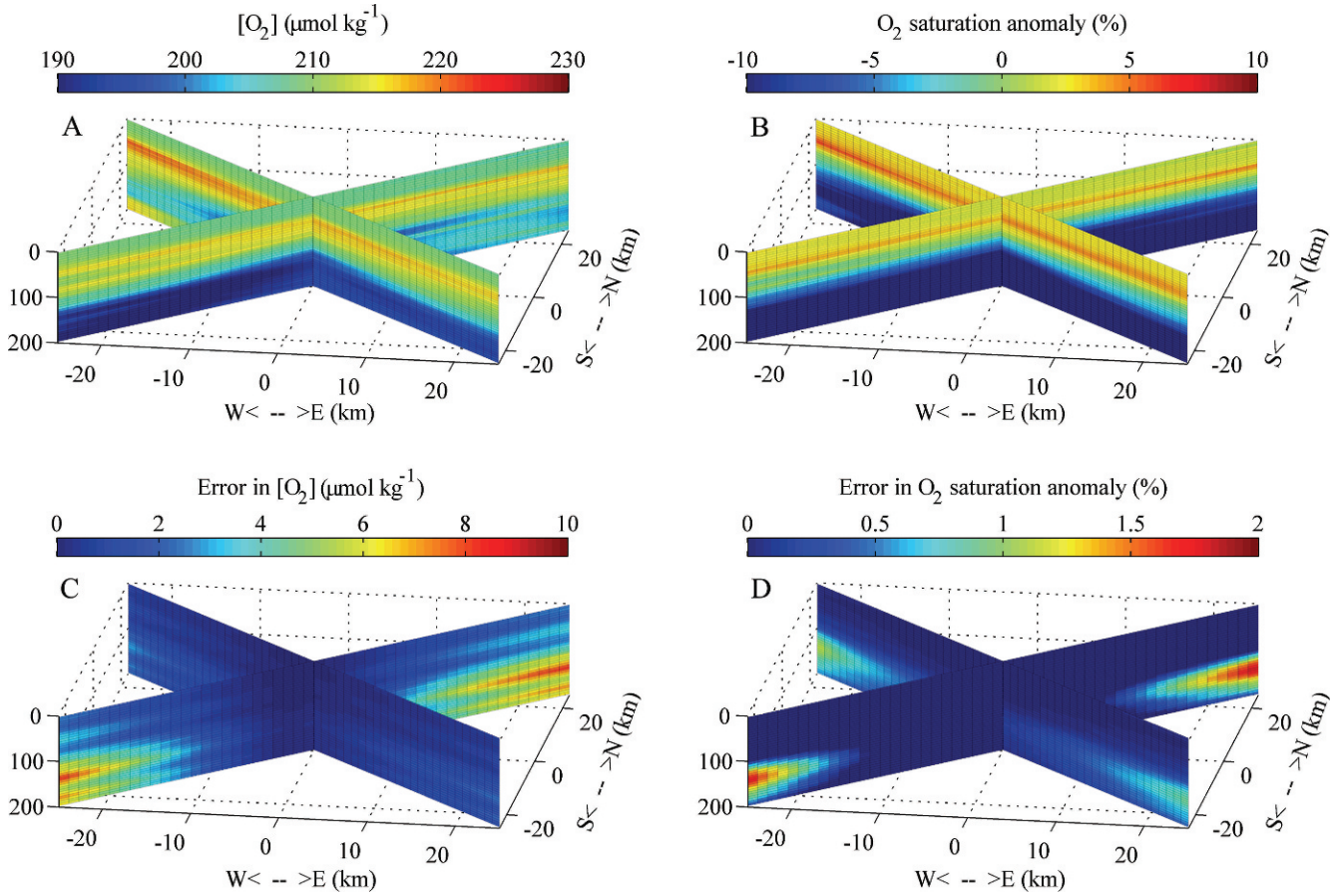

Fig. 7. A visualization for 02 July 2005 of (A) O_2 concentration (μmol kg^{-1}) mapped on depth surfaces, (B) O_2 saturation anomaly (percent) and (C and D) the corresponding error maps. Areas of higher error correspond to the regions that were far away from the Seaglider's flight path around 02 July 2005 when the Seaglider was near Station ALOHA and traveling from southeast to northwest. Error is greater at depths where $[O_2]$ are highly variable.

maximum was weakening but still present. Presumably deep, winter mixing between November and February would eliminate this feature and return the O_2 profile to values similar to the conditions at the onset of the study.

Productivity in the deep euphotic zone—A significant portion of productivity at Station ALOHA occurs at depth, near the base of the photic zone (Letelier et al. 2004). A deep chlorophyll maximum layer (DCML) is present through the year. In a downwelling, oligotrophic environment such as the subtropical gyres there is a limited supply of nutrients. Autotrophs positioned at the base of the euphotic zone, while pushing the limitations of light availability, are closer to sources of deep, nutrient-rich water. In fact, the changing depth of the nutricline corresponds with seasonally migrating isolums. As light penetrates deeper in the water column during summer, the DCML moves lower, and the nutricline is displaced downward as well (Winn et al. 1995).

The mechanism for nutrient transport from deeper, nutrient-rich waters into the euphotic zone is poorly understood (Hayward and McGowan 1982; McGillicuddy et al. 2003; Sakamoto et al. 2004). Upward nutrient flux by turbulent mixing has been shown in models to be insufficient to support the levels of NCP that have been observed (Hayward and McGowan 1982). Mesoscale eddy activity has been hypothesized to be important sources of nutrients, and observations have correlated remotely sensed ocean color to Rossby wave–induced SSH anomalies (Killworth et al. 2004). Evidence for Rossby wave activity can be seen in SSH altimetry that reveals westward propagating peaks and troughs traveling across the Pacific (Fig. 5). We observed a correspondence between SSH anomalies at Station ALOHA and the depth of isotherms: when SSH was high, isopycnals were deep, and vice versa (Fig. 8). This relationship suggests that isopycnal variations are largely due to cyclonic and anticyclonic flows associated with mesoscale events.

At Station ALOHA, we identified four events of isopycnal shoaling in the SSH data (Fig. 5). These events showed up as lows in SSH, and we expected that they also would have an associated cyclonic flow and shoaling of isopycnals at depth. The first event happened from day 50 to day 70, the second event happened from day 100 to day 120, the third and largest event happened from day 150 to day 180, and the final event happened from day 290 to day 310.

Seaglider $[O_2]$ and fluorescence data can be used as indicators of productivity caused by eddy- and Rossby-

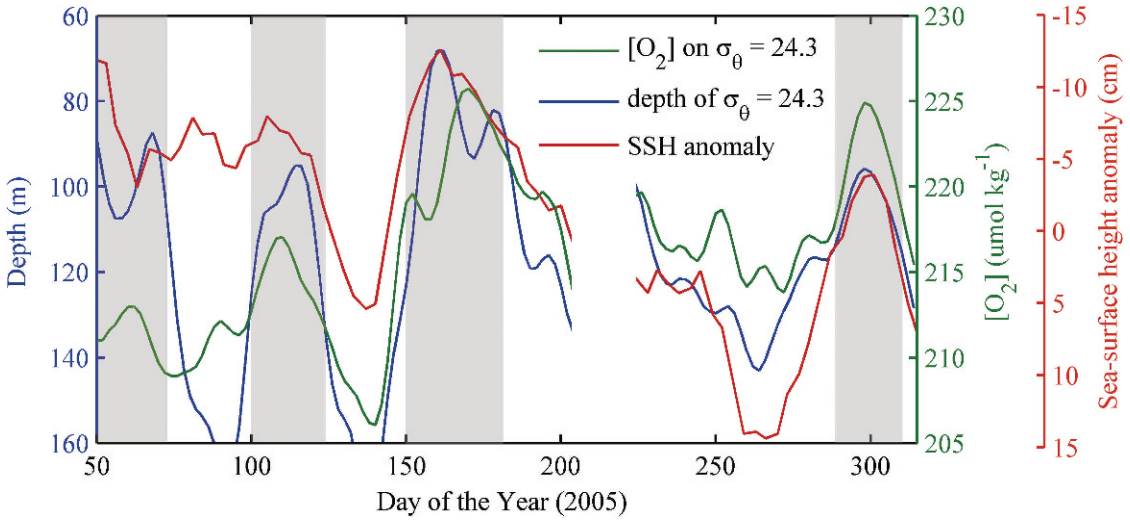

Fig. 8. The depth of isopycnal σ_θ = 24.30 measured by Seagliders (blue), sea-surface height anomalies at Station ALOHA (red), from Ssalto/Duacs merged altimetry, and $[O_2]$ concentration mapped on σ_θ = 24.30 (green). The gray shading indicates the four productivity events.

induced vertical displacements of isopycnals. $[O_2]$ mapped onto σ_θ = 24.30 shows a strong relationship with the depth of the σ_θ = 24.30 isopycnal (Fig. 8). When the isopycnal shoals, i.e., during the passage of each of the four mesoscale events, $[O_2]$ on that isopycnal is higher. This indicates an increase in photosynthetically produced O_2 due to increased light availability as water is raised higher into the euphotic zone and increased respiration when isopycnals are deep.

Further evidence that shoaling isopycnals stimulate biological activity is seen in fluorescence data. Fluorescence is an indicator of the presence of chlorophyll *a* in the water column. In the deep euphotic zone, at Station ALOHA, changes in fluorescence have been demonstrated to be due to changes in primary productivity in this zone (Winn 1995). While the Seaglider fluorescence did not give us absolute chlorophyll *a* concentrations, we interpreted changes in fluorescence intensity in the deep euphotic zone to represent changes in the relative rate of primary productivity in this region. Intensity of fluorescence measured by the Seaglider near the base of the euphotic zone, at 117.5 m, is correlated with the depth of isopycnals in this region (Fig. 9). During each of the four mesoscale events, fluorescence increased, not just at 117.5 m, but throughout the DCML (Fig. 9).

Deep euphotic zone NCP from an O_2 mass balance—If productivity in the deep euphotic zone is driven by inputs of nutrients from beneath the euphotic zone, this represents NCP and should be associated with a net production of biological O_2. An O_2 mass balance of the zone below the mixed layer but still within the euphotic zone can be used to determine the net biological O_2 production and thus NCP beneath the mixed layer. Two likely fates of biologically produced O_2 in the deep euphotic zone are loss to the mixed layer by entrainment and transport to the thermocline by turbulent diffusion. To calculate the amount of O_2 that is biologically produced below the mixed layer and above σ_θ = 24.30, we used a mass balance of O_2 that included the O_2 inventory, entrainment, and vertical mixing.

Our O_2 mass balance of the deep euphotic zone extends from the base of the mixed layer down to σ_θ = 24.30. The base of the O_2 mass balance domain was chosen to closely correspond with the base of the euphotic zone. During the study period σ_θ = 24.30 had a mean depth of 118 m, and the level of 1% photosynthetically active radiation at Station ALOHA varied from 105 m in winter to 121 m in the summer (Letelier et al. 2004). An isopycnal base was chosen to minimize the effect on the O_2 balance of vertical isopycnal displacement due to mesoscale variability. Using an isobath base would have resulted in low-O_2 water moving in and out of the mass balance volume with the passage of mesoscale features. Because the thickness of the deep euphotic zone's mass balance is variable with time, the O_2 inventory is calculated by multiplying the average $[O_2]$ in this layer by the mean thickness of the layer (64.3 m). The budget is thus normalized to the mean thickness of the deep euphotic zone layer.

Assuming that one-dimensional processes dominate, the amount of O_2 produced biologically, $J_{\mathrm{Bio-O_2}}$, can be calculated for each time step from the O_2 inventory and the contribution of fluxes across the upper and lower boundaries due to turbulent mixing and mixed-layer entrainment such that,

$$J_{\mathrm{Bio-O_2}} = dt\left(\bar{z}_{\mathrm{deep}} d\overline{[O_2]} - \bar{z}_{\mathrm{deep}} E_{O_2} - K_z\left[\frac{\partial [O_2]}{\partial z}\right]_{\sigma_\theta\,=\,\mathrm{base}}\right), \quad (9)$$

where $\bar{z}_{\mathrm{deep}}$ is the mean thickness of the deep euphotic zone; $d\overline{[O_2]}$is the change in average $[O_2]$ of the layer, and E_{O_2} describes the effect of entrainment when the mixed layer deepens, incorporating a portion of the high-O_2 layer below. The flux of O_2 due to turbulent diapycnal mixing is $dtK_z\frac{\partial [O_2]}{\partial z}$ and depends on the vertical O_2 gradient, and the coefficient for turbulent diffusivity, K_z.

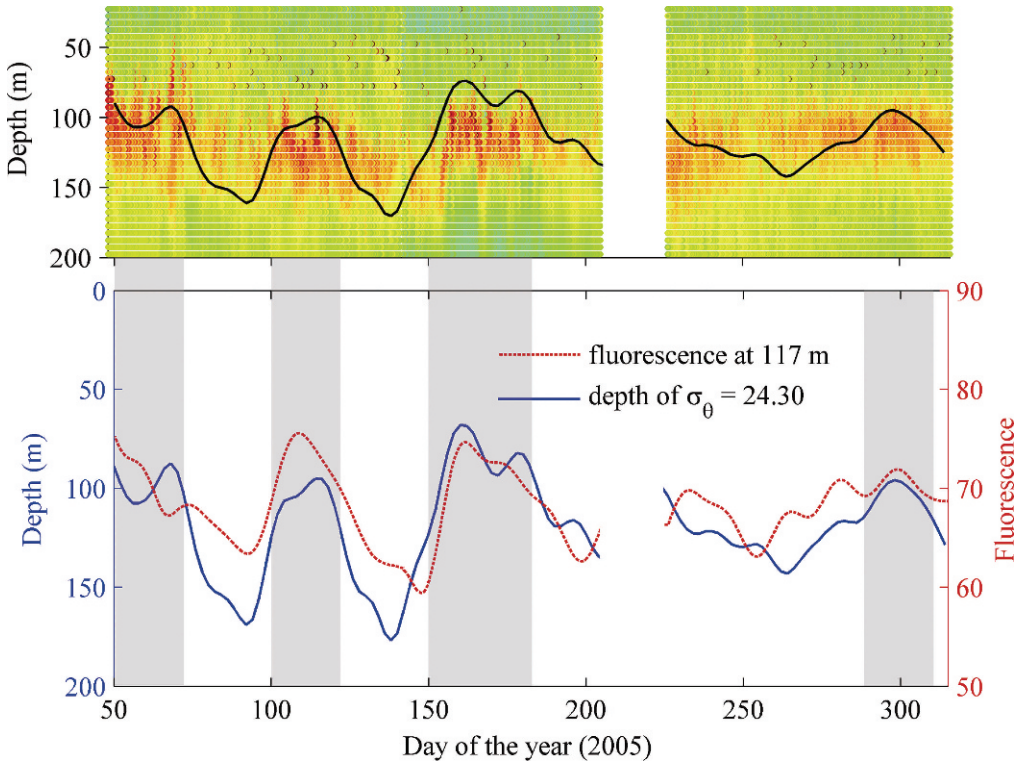

Fig. 9. Seaglider measured fluorescence in the upper 200 m at Station ALOHA (above) with red colors indicating higher values. Below, the depth of $\sigma_\theta = 24.30$ at the center grid point (black) is compared to low-pass filtered fluorescence at 117 meters (dashed). Peaks in fluorescence are observed during all four of the productivity events (gray shading).

Entrainment was calculated for each time step in the mass balance when the depth of the mixed-layer increases. When the mixed layer deepens, the water directly beneath it is entrained into the mixed layer and lost from the deep euphotic zone. Because $[O_2]$ varies with depth, this process can either increase or decrease the average $[O_2]$ in the deep euphotic zone The amount that entrainment changes the average $[O_2]$ of the deep euphotic zone, E_{O_2}, is calculated as

$$E_{O_2} = \frac{dz_{ml}}{dt}\left([O_2]_{\text{entrain}} - [O_2]_{\text{deep}}\right) \Big/ \left(\bar{z}_{\text{deep}}\right) \qquad (10)$$

where dz_{ml} is the change in the depth of the mixed layer, $[O_2]_{\text{entrain}}$ is the mean concentration of the water that is entrained, $[O_2]_{\text{deep}}$ is the mean concentration of the deep euphotic zone, and dt is the time step.

By evaluating the terms in Eq. 9, we calculate a time series of $J_{\text{Bio}-O_2}$, the net biological O_2 production (Fig. 10). The increase in biologically produced O_2 with time is evident whether a mixing flux is present or not. A mass budget considering only O_2 inventory and entrainment results in an annual biological O_2 production of 0.9 $\pm$ 0.1 mol O_2 m^{-2} yr^{-1}. Adding a mixing flux with K_z = 1.0 cm^2 s^{-1} contributes an additional 0.6 mol O_2 m^{-2} yr^{-1} of net biological O_2 production. A value of 1.0 cm^2 s^{-1} is the upper bound of the range of values typically used in previous studies (e.g., Hamme and Emerson 2006). Thus, 0.9 mol O_2 m^{-2} yr^{-1} and 1.5 mol O_2 m^{-2} yr^{-1} can be considered to be the lower and upper bounds of our estimate of net biological O_2 production in the deep euphotic zone. Riser and Johnson (2008) calculated NCP for the deep euphotic zone near Hawaii using profiling floats. They found a maximum NCP of 15 mmol C m^{-2} yr^{-1} beneath the mixed layer. Extrapolated across the deep euphotic zone, this is equivalent to 1.4 mol O_2

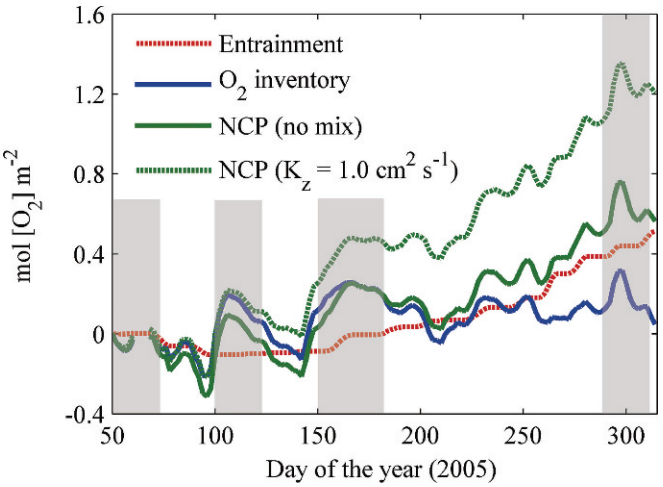

Fig. 10. O_2 budget for the deep euphotic zone, between the base of the mixed layer and $\sigma_\theta = 24.30$. Inventories are multiplied by the mean thickness of this layer to give units of mol O_2 m^{-2}. The inventory plus entrainment (solid green) is a lower bound estimate of biological O_2 production while adding mixing provides an upper bound estimate (dashed green). The four productivity events (gray shading) all align with periods of increased NCP.

m^{-2} yr^{-1}, close to the upper limit of our estimate. As is evident from Fig. 10, these rates of biological O_2 production are not steady through the year. During the four periods of shoaling isopycnals, biological O_2 production and NCP is elevated. When isopycnals fall, the opposite is the case, and the deep euphotic zone appears to often be net heterotrophic during these periods.

The Seaglider survey thus clearly demonstrates the importance of Rossby waves in driving the large vertical displacements in isopycnal depth that regulated NCP in the deep euphotic zone.

References

Anderson, L. A. 1995. On the hydrogen and oxygen content of marine phytoplankton. Deep-Sea Res. I **42:** 1675–1680.

Bretherton, F. P., R. E. Davis, and C. B. Fandry. 1976. A technique for objective analysis and design of oceanographic experiments applied to MODE-73. Deep-Sea Res. **23:** 559–582.

Clark, L. C., R. Wolf, D. Granger, and Z. Taylor. 1953. Continuous recording of blood oxygen tensions by polarography. J. Appl. Physiol. **6:** 189–193.

Chelton, D. B., and M. G. Schlax. 1996. Global observations of oceanic Rossby waves. Science **272:** 234–238, doi: 10.1126/science.272.5259.234.

Chiswell, S. M. 1994. Using an array of inverted echo sounders to measure dynamic height and geostrophic current in the North Pacific subtropical gyre. J. Atmos. Oceanic Tech. **100:** 1420–1424.

Duarte, C. M., and S. Agusti. 1998. The CO_2 balance of unproductive aquatic ecosystems. Science **281:** 234–236.

Del Giorgio, P. A., and C. M. Duarte. 2002. Respiration in the open ocean. Nature **420:** 379–384.

Emerson, S., P. Quay, D. Karl, C. Winn, L. Tupas, and M. Landry. 1997. Experimental determination of the organic carbon flux from open-ocean surface waters. Nature **389:** 951–954.

———, C. Stump, B. Johnson, and D. M. Karl. 2002. In situ determination of oxygen and nitrogen dynamics in the upper ocean. Deep-Sea Res. I **49:** 941–952.

———, ———, and D. Nicholson. In press. Net biological oxygen production in the ocean: remote in-situ measurements of O_2 and N_2 in surface waters. Global Biogeochem. Cycles, doi: 10.1029/2007GB003095.

Eriksen, C. C., and others. 2001. Seaglider: a long-range autonomous underwater vehicle for oceanographic research. IEEE J. Oceanic Eng. **26:** 424–436.

Gruber, N., C. D. Keeling, and T. F. Stocker. 1998. Carbon-13 constraints on the seasonal inorganic carbon budget at the BATS site in the northwestern Sargasso Sea. Deep-Sea Res. I **45:** 673–717.

Hamme, R., and S. Emerson. 2006. Constraining bubble dynamics and mixing with dissolved gases: Implications for productivity measurements by oxygen mass balance. J. Mar. Res. **64:** 73–95.

Hayward, T. L., and J. A. McGowan. 1982. Spatial patterns of chlorophyll, primary production, macrozooplankton biomass, and physical structure in the central North Pacific Ocean. J. Plankton Res. **7:** 147–167.

Hedges, J. I., J. A. Baldock, Y. Gelinas, C. Lee, M. L. Peterson, and S. G. Wakeham. 2002. The biochemical and elemental compositions of marine plankton: A NMR perspective. Mar. Chem. **78:** 47–63.

Killworth, P. D., P. Cipollini, B. M. Uz, and J. R. Blundell. 2004. Physical and biological mechanisms for planetary waves observed in satellite-derived chlorophyll. J. Geophys. Res. **109:** C07002, doi:10.1029/2003JC001768.

Körtzinger, A. 2005. High quality oxygen measurements from profiling floats: A promising new technique. J. Atmos. Oceanic Tech. **22:** 302–308. doi: 10.1175/JTECH1701.1.

Laws, E. A. 1991. Photosythetic quotients, new production and net community production in the open ocean. Deep-Sea Res. **38:** 143–167.

Letelier, R. M., D. M. Karl, M. R. Abbott, and R. R. Bidigare. 2004. Light driven seasonal patterns of chlorophyll and nitrate in the lower euphotic zone of the North Pacific subtropical gyre. Limnol. Oceanogr. **49:** 508–519.

Le Traon, P. Y. 1990. A method for optimal analysis of fields with spatially variable mean. J. Geophys Res. **95:** 13543–13547.

McAndrew, P. M., and others. 2007. Metabolic response of oligotrophic plankton communities to deep water nutrient enrichment. Mar. Ecol. Prog. Ser. **332:** 63–75.

McGillicuddy, D. J., L. A. Anderson, S. C. Doney, and M. E. Maltrud. 2003. Eddy-driven sources and sinks of nutrients in the upper ocean: Results from a 0.1° resolution model of the North Atlantic. Global Biogeochem. Cycles **17:** 1035. doi: 10.1029/2002GB001987.

Quay, P., and J. Stutsman. 2003. Surface layer carbon budget for the subtropical North Pacific: δ13C constraints at station ALOHA. Deep-Sea Res. I **50:** 1045–1061.

Polito, P. S., and W. T. Liu. 2003. Global characterization of Rossby waves at several spectral bands. J. Geophys. Res. **108:** 3018, doi:10.1029/2000JC000607.

Riser, S. C., and K. S. Johnson. 2008. Net production of oxygen in the subtropical ocean. Nature **451:** 323–325, doi:10.1038/nature06441.

Sakamoto, C. M., and others. 2004. Influence of Rossby waves on nutrient dynamics and the plankton community structure in the North Pacific subtropical gyre. J. Geophys. Res. **109:** C05032.

Seckel, G. R. 1968. A time-sequence oceanographic investigation in the North Pacific trade-wind zone. Trans. Am. Geophys. Union **49:** 377–386.

Spitzer, W. S., and W. J. Jenkins. 1989. Rates of vertical mixing, gas exchange and new production: Estimates from seasonal gas cycles in the upper ocean near Bermuda. J. Mar. Res. **47:** 169–196.

Sweeney, E. N., D. J. McGillicuddy, Jr., and K. O. Buesseler. 2003. Biogeochemical impacts due to mesoscale eddy activity in the Sargasso Sea as measured at the Bermuda Atlantic Time-series Study (BATS). Deep-Sea Res. II **50:** 3017–3039.

Tengberg, A., and others. 2006. Evaluation of a lifetime-based optode to measure oxygen in aquatic systems. Limnol. Oceanogr. Methods **4:** 7–17.

Williams, J. le B., P. J. Morris, and D. M. Karl. 2004. Net community production and metabolic balance at the oligotrophic ocean site, station ALOHA. Deep-Sea Res. I **51:** 1563–1578.

Winn, C. D., and others. 1995. Seasonal variability in the phytoplankton community of the North Pacific subtropical gyre. Global Biogeochem. Cycles **9:** 605–620.

Received: 9 October 2007
Accepted: 18 April 2008
Amended: 30 April 2008